MATERIALS SCIENCE

Li substituent tuning of LED phosphors with enhanced efficiency, tunable photoluminescence, and improved thermal stability

Ming Zhao[1], Zhiguo Xia[1,2]*, Xiaoxiao Huang[3], Lixin Ning[3]*, Romain Gautier[4], Maxim S. Molokeev[5,6,7], Yayun Zhou[2], Yu-Chun Chuang[8], Qinyuan Zhang[2], Quanlin Liu[1], Kenneth R. Poeppelmeier[9]*

Solid-state phosphor-converted white light-emitting diodes (pc-WLEDs) are currently revolutionizing the lighting industry. To advance the technology, phosphors with high efficiency, tunable photoluminescence, and high thermal stability are required. Here, we demonstrate that a simple lithium incorporation in $NaAlSiO_4$:Eu system enables the simultaneous fulfillment of the three criteria. The Li substitution at Al sites beside Na sites in $NaAlSiO_4$:Eu leads to an enhanced emission intensity/efficiency owing to an effective Eu^{3+} to Eu^{2+} reduction, an emission color tuning from yellow to green by tuning the occupation of different Eu sites, and an improvement of luminescence thermal stability as a result of the interplay with Li-related defects. A pc-WLED using the Li-codoped $NaAlSiO_4$:Eu as a green component exhibits improved performance. The phosphors with multiple activator sites can facilitate the positive synergistic effect on luminescence properties.

INTRODUCTION

Energy-efficient white light-emitting diodes (WLEDs) are widely used in modern lighting technology and backlit displays, which are typically composed of a blue or ultraviolet (UV) pumping LED and one or more phosphors (1–3). The requirements for phosphors in LED applications mainly include (i) high luminescence quantum efficiency (QE), (ii) tunable photoluminescence (PL) properties for different devices, and (iii) maintenance of emission intensity at elevated temperatures, especially for high-power or laser LED applications (4–8). Phosphors are generally developed by appropriate selection of inorganic matrices and doped activators (9). However, such a design is difficult because the PL properties are hardly predictable. Thus, modification of local environments of activators by chemical substitutions becomes an essential approach to optimize previously reported phosphors (10, 11). In general, one can increase the efficient dopant concentration to enhance the PL efficiency, modify the amount of activators in different sites to vary the emission color, and change the host composition to reduce thermal quenching (12–14). While different approaches have been used to achieve one or two of the objectives in most cases, none has efficiently tackled the three issues using one single strategy to the best of our knowledge (15, 16).

To "kill three birds with one stone," we decided to develop an approach in which the three objectives could be possibly achieved by lithium incorporation into one preselected phosphor system. Our method consists first of the selection of the appropriate host matrix and dopant for which the Li codoping would lead to a tuning of activator concentration (challenge 1), a modification of activator site distribution (challenge 2), and a promotion of thermal stability of activator emission (challenge 3). Thus, we selected $NaAlSiO_4$:Eu because the structure of this compound exhibits different cations' crystallographic sites in which Eu could be located and the relative ratio Eu^{2+}/Eu^{3+} could be tuned to enhance the PL intensity. Hence, depending on the variation of Li doping concentration, the phosphors show PL tuning from yellow to green emission corresponding to an increase of Eu^{2+} occupation ratio at Na1 sites (~450 nm) relative to Na2 sites (~535 nm). In addition, the emission intensities increase and, accordingly, QE is improved due to the reduction of Eu^{3+} to Eu^{2+}. The thermal stability is also enhanced due to the positive effect induced by Li incorporation. This investigation is expected to initiate more exploration into the positive effects of heterovalent doping on luminescence properties of phosphors by tailoring crystallographic sites of activators and regulating their local structures.

RESULTS AND DISCUSSION

Doping effect on the crystal structure of $NaAlSiO_4$

The nepheline polymorphic form of $NaAlSiO_4$ was first studied without Li addition. Both $Na_{(1-x)}\square_{(x)}Al_{(1-x)}Si_{(1+x)}O_4$ (abbreviated as N$\square_x$ASO, where $\square$ represents Na vacancy, V_{Na}) and $Na_{(0.99-x)}\square_{(x)}Al_{(1-x)}Si_{(1+x)}O_4$:0.01Eu (abbreviated as N$\square_x$ASO:Eu) samples were designed and prepared with $x = 0$, 0.05, 0.1, 0.15, 0.20, and 0.25. On the basis of the Rietveld analysis from laboratory powder x-ray diffraction (PXRD) (fig. S1), it was found that the materials with substoichiometric Na content and with Eu dopants do not generate any impurity phases when x is below 0.25. Moreover, the unit cell volume (V) increased with increasing x for the two series of samples, in agreement with previous work (Fig. 1A) (17, 18). The nonlinear increase of the cell volume with x could be due to an inhomogeneous redistribution of Si in the two crystallographic sites of Al. For N$\square_x$ASO:Eu, the obtained cell volumes (see details in table S1) are larger than those of corresponding N$\square_x$ASO

[1]The Beijing Municipal Key Laboratory of New Energy Materials and Technologies, School of Materials Sciences and Engineering, University of Science and Technology Beijing, Beijing 100083, China. [2]State Key Laboratory of Luminescent Materials and Devices and Institute of Optical Communication Materials, South China University of Technology, Guangzhou 510641, China. [3]Anhui Key Laboratory of Optoelectric Materials Science and Technology, Key Laboratory of Functional Molecular Solids, Ministry of Education, Anhui Normal University, Wuhu, Anhui 241000, China. [4]Institut des Matériaux Jean Rouxel (IMN), Université de Nantes, CNRS, 2 rue de la Houssinière, BP 32229, 44322 Nantes, Cedex 03, France. [5]Laboratory of Crystal Physics, Kirensky Institute of Physics, Federal Research Center KSC SB RAS, Krasnoyarsk 660036, Russia. [6]Siberian Federal University, Krasnoyarsk 660041, Russia. [7]Department of Physics, Far Eastern State Transport University, Khabarovsk 680021, Russia. [8]National Synchrotron Radiation Research Center, Hsinchu 300, Taiwan. [9]Department of Chemistry, Northwestern University, 2145 Sheridan Road, Evanston, IL 60208-3113, USA.
*Corresponding author. Email: xiazg@ustb.edu.cn (Z.X.); ninglx@mail.ahnu.edu.cn (L.N.); krp@northwestern.edu (K.R.P.)

samples, in good agreement with the larger ion radius of Eu^{2+} [1.25 Å @ coordination number (CN) = 8] than that of Na^+ (1.18 Å @ CN = 8).

For the samples with Li doping, the PXRD patterns of $Na_{(0.99-x)}\square_{(x)}Al_{(1-x)}Si_{(1+x)}O_4$:$y$Li, 0.01Eu (abbreviated as N$\square$ASO:yLi, Eu) ($x = y$, $0 \leq y \leq 0.15$) were collected (Fig. 1B) and indexed using a hexagonal cell $P6_3$ with parameters close to the nepheline $NaAlSiO_4$ [powder diffraction file (PDF) card no. 35-0424] [8, 19]. Moreover, the synchrotron x-ray diffraction (SXRD) data were collected and the Rietveld refinements of the series of N$\square$ASO:yLi, Eu ($x = y = 0$, 0.05, 0.10, 0.15) (fig. S2 and table S2) confirmed the absence of impurities and the structural parameters. The cell volume increases nonlinearly with increasing Li doping concentration (y) (Fig. 1C), which suggests that Li could be partly located (or inserted) at sites other than Na sites. To further confirm the local structures of Li, Al, and Si atoms in N$\square$ASO:yLi, Eu ($y = 0$, 0.12), ^{7}Li, ^{27}Al, and ^{29}Si solid-state nuclear magnetic resonance

(NMR) was performed. The ^{7}Li NMR spectrum of N$\square$ASO:yLi, Eu ($y = 0.12$) (Fig. 2I) shows two signals with maxima at 0.696 ppm/−0.159 ppm, indicating the existence of at least two substitution/insertion sites, in agreement with the nonlinear evolution of cell volume with increasing Li amount as observed in SXRD. The ^{27}Al NMR spectra show two signals at 60.91 ppm/65.93 ppm for N$\square$ASO:yLi, Eu ($y = 0$) and 61.21 ppm/66.01 ppm for N$\square$ASO:yLi, Eu ($y = 0.12$) (fig. S3, A and C). This result agrees with the presence of two distinct Al crystallographic sites in the configuration Q^4(4Si) (each Al is coordinated by four Si through corner-sharing oxygen atoms) (20). The ^{29}Si solid-state NMR spectra of N$\square$ASO:yLi, Eu ($y = 0$, 0.12) (fig. S3, B and D) show two main peaks at −84.31 ppm/−89.11 ppm for $y = 0$ and −84.23 ppm/−88.73 ppm for $y = 0.12$. These values are similar to the ones obtained previously for nepheline $NaAlSiO_4$ (−85 ppm/−89 ppm) (20). The difference between chemical shifts of Si1 and Si2 can be associated with

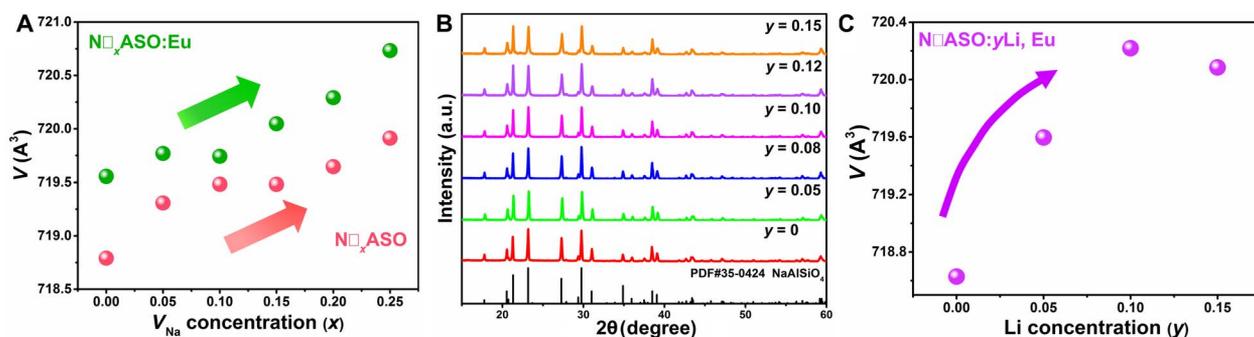**Fig. 1. Structural characterization of N$\square_x$ASO, N$\square_x$ASO:Eu, and N$\square$ASO:yLi, Eu phosphors.** (**A**) Dependence of unit cell volume (V) on the V_{Na} concentration (x) of N$\square_x$ASO and N$\square_x$ASO:Eu ($0 \leq x \leq 0.25$) obtained from PXRD patterns. a.u., arbitrary units. (**B**) PXRD patterns of N$\square$ASO:yLi, Eu ($0 \leq y \leq 0.15$). All diffraction peaks match well with the standard patterns of nepheline $NaAlSiO_4$ (PDF card no. 35-0424). (**C**) Dependence of unit cell volume (V) on the Li doping concentration (y) of N$\square$ASO:yLi, Eu ($0 \leq y \leq 0.15$).

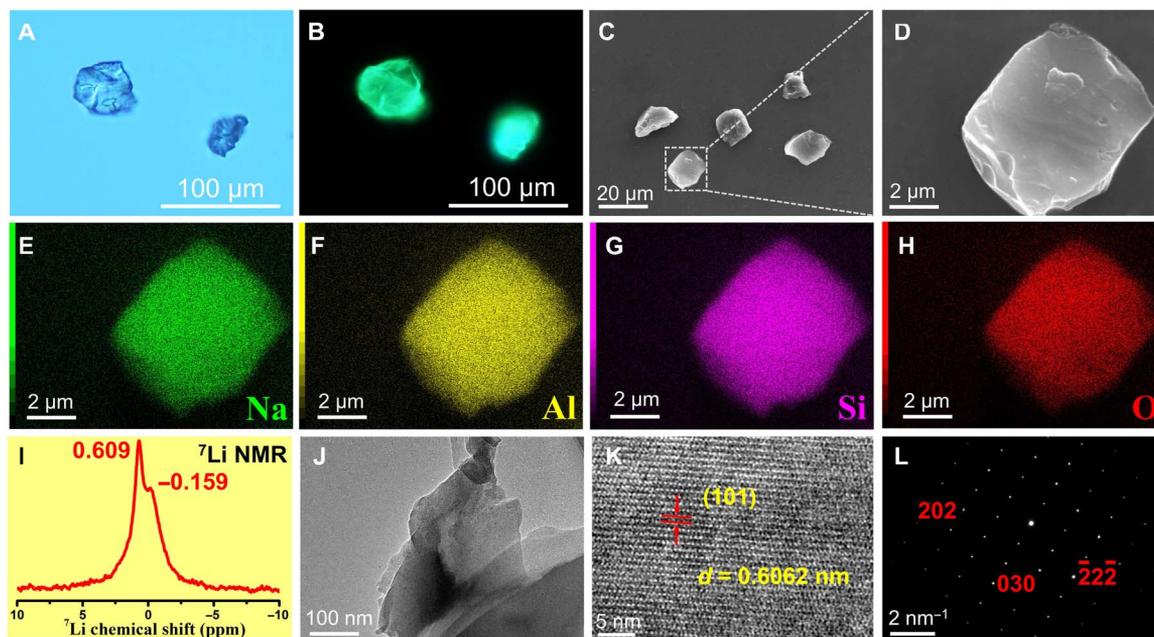**Fig. 2. Morphology and composition of N$\square$ASO:yLi, Eu ($y = 0.10$) phosphor.** Optical microscope photographs of the N$\square$ASO:yLi, Eu ($y = 0.10$) microcrystal particles (**A**) without and (**B**) with 365-nm UV excitation. (**C**) SEM images of N$\square$ASO:yLi, Eu ($y = 0.10$) microcrystal particles and (**D**) an enlarged particle. (**E** to **H**) Element mapping images of Na, Al, Si, and O in the selected N$\square$ASO:yLi, Eu ($y = 0.10$) particle. (**I**) ^{7}Li solid-state NMR spectrum of N$\square$ASO:yLi, Eu ($y = 0.12$). (**J** to **L**) TEM and HRTEM images of the selected area and the corresponding SAED of N$\square$ASO:yLi, Eu ($y = 0.10$). The SAED image was detected in the zone axis [10$\bar{1}$] orientation.

the second coordination sphere. The two observed signals are consistent with the presence of two different Si crystallographic sites in the nepheline crystal structure. Moreover, the ^{29}Si peak position of the four-coordinated Si (SiO$_4$) is located at about −82 to −92 ppm for Q^4(4Al) (20), also in good agreement with our experimental data. ^{27}Al and ^{29}Si NMR indicate that the CNs of Al and Si atoms in the crystal structures are equal to 4, which are consistent with the crystal structures. However, the Li$^+$ doping and Na$^+$ decreasing at low concentration only slightly changes the chemical shifts of ^{27}Al and ^{29}Si. Hence, to further investigate the effect of Na$^+$ decreasing on Al and Si sites, ^{27}Al and ^{29}Si solid-state NMR of N□$_x$ASO (x = 0.05, 0.10, 0.15, and 0.25) were measured. As shown in fig. S3E, the ^{27}Al NMR spectra show two signals located at about 62 to 72 ppm, and the ^{29}Si solid-state NMR spectra (fig. S3F) show two main peaks located at about −82 to −92 ppm. These results confirm that two different Al and Si sites exist in the structures, and the CNs of Al and Si atoms in the crystal structures are still equal to 4. Moreover, the peak intensities of Al and Si varied gradually with decreasing Na concentration, indicating the change of Al and Si contents in the system. It implies that Si$_{Al}$ substitutions are present in N□$_x$ASO to compensate for the reduced charge owing to Na vacancies.

Figure 2 (A and B) represents the optical microscope photographs of the selected N□ASO:yLi, Eu (y = 0.10) without and with 365-nm UV light excitation, respectively. Under the UV excitation, a bright green emission (Fig. 2B) can be observed for N□ASO:yLi, Eu (y = 0.10) phosphor. Scanning electron microscope (SEM) images of this sample (Fig. 2, C and D) show particle sizes of 10 to 20 μm with high crystallinity. Moreover, the energy-dispersive x-ray spectroscopy (EDS) elemental mapping technique was used to confirm the composition uniformity of N□ASO:yLi, Eu (y = 0.10), as shown in Fig. 2 (E to H). The elemental mapping images exhibit that Na, Al, Si, and O are very homogeneously distributed within the phosphor particles. Figure 2J presents the morphology of the sample, and its fine structure is further examined by high-resolution transmission electron microscope (HRTEM), as shown in Fig. 2K, indicating the continuous lattice fringe measurements with d spacing of 0.6062 nm for the (101) plane, which agrees with the refined structure of nepheline phase. The selected-area electron diffraction (SAED) pattern taken along the [10$\bar{1}$] zone axis of the sample is shown in Fig. 2L, confirming the hexagonal crystal structure of the compound.

Li Occupation in NaAlSiO$_4$

To better understand Li incorporation in N□ASO, density functional theory (DFT) energetic calculations were performed to compare the occurrence probabilities of a Li substituted at a Na or Al site. In the $1 \times 1 \times 2$ supercell model for undoped N□ASO, there are four Na1 sites in a line along the c axis and 12 Na2 sites. Two of the four Na1 sites were set to be vacant (V_{Na1}) in accordance with experiments (8) and were placed at alternative (rather than neighbor) positions because the agglomeration of the vacancies was not observed experimentally. To maintain the charge neutrality of the system, two additional Si$_{Al}$ substitutions were introduced and there are, in principle, (16)!/(14!×2!) = 120 different Si$_{Al}$-Si$_{Al}$ configurations in the supercell. When the crystal symmetry was taken into account (21), the number of crystallographically distinct configurations necessary for calculations reduced to 12. The occurrence probabilities P_i (i = 1, …, 12) of these configurations were then determined by $P_i = \frac{1}{z_{tot}} \Omega_i \exp\left(-\frac{E_i}{kT}\right)$, where z_{tot} is the partition function, Ω_i is the multiplicity, E_i is the DFT total energy, k is the Boltzmann constant, and T (= 1473 K) is the synthesis temperature of the material. DFT calculations revealed that there are three distinct configurations

constituting the major portion of the total ensemble, with the occurrence probabilities P = 0.224, 0.217, and 0.207, respectively. The probabilities for the other inequivalent configurations are each lower than 0.1. The undoped supercells with these three most probable configurations were used for subsequent investigations of Li$^+$ and Eu^{2+} site occupations in the host.

We first calculated the defect formation energies for a Li substituted at Na sites (Li$_{Na}$), which can be described by the formula Li + N□ASO → N□ASO:Li$_{Na}$ + Na, where N□ASO denotes the reference supercell and N□ASO:Li$_{Na}$ is the Li$_{Na}$-doped supercell. From DFT total energies, the formation energies for a Li substituted at each of the 42 Na sites in the three reference supercells were predicted to be in the range from −0.412 to 0.073 eV. The negative values indicate that the substitutions are thermodynamically favorable. Second, we considered the substitutions of a Li at an Al site, with the excess charge compensated by two additional Li atoms intercalated at the two V_{Na1} sites. This scenario can be expressed as follows: 3Li + N□ASO → N□ASO:Li$_{Al}$-2Li$_{V_{Na1}}$ + Al. For the 42 Al sites present in the three reference supercells, the calculated defect formation energies per Li are in the range from −0.371 to 0.013 eV. Last, to compare the relative preference of the above two ways of Li incorporation, the occurrence probability for each Li substitution was calculated by using $P_j = \frac{1}{z_{tot}} \exp\left(-\frac{E_j}{kT}\right)$, ($j$ = 1, …, 84), where E_j is the defect formation energy. By summing the 42 values of P_j for Li$_{Al}$-2Li$_{V_{Na1}}$ and Li$_{Na}$ substitutions, respectively, we found that Li has a higher tendency to be at the Al site than at the Na site, with the overall probabilities being 0.615 and 0.385, respectively. For the comparison, we have additionally investigated the Li substitutions at each of the 42 Al sites with a nearest-neighbor V_O for charge compensation and the Li intercalation at the 12 interstitial sites with the largest voids. The calculated defect formation energies are mostly positive, and thus, these incorporations are thermodynamically unfavorable. These theoretical results also indicate that the Na1 deficiency in the host material plays an important role in favoring Li substitutions at Al sites. Besides the results of defect formation energies, DFT calculations show that most Li$_{Al}$-2Li$_{V_{Na1}}$ substitutions in N□ASO led to an increase (by at most 0.89%) of the supercell volume, whereas all the Li$_{Na}$ substitutions caused a decrease (by at most 1.30%) of the supercell volume. In view of the higher overall occurrence probability of the former type of substitutions than the latter type, we expect that Li incorporation in N□ASO would result in an expansion of the unit cell. Thus, the experimental observations (Fig. 1C) would suggest that Li$_{Al}$-2Li$_{V_{Na1}}$ substitution is predominant over Li$_{Na}$ substitution.

Challenge 1: To enhance emission intensity/efficiency

The PL and PL excitation (PLE) spectra of N□ASO:yLi, Eu ($0 \le y \le 0.15$) phosphors are shown in Fig. 3 (A and B), respectively. Under excitation at 365 nm, the N□ASO:yLi, Eu (y = 0) phosphor exhibits a broad band consisting of a dominant peak at ~535 nm and a minor shoulder peak at ~450 nm. The corresponding PLE spectrum monitored at 535 nm exhibits a broad band with two main peaks at 275 and 325 nm, respectively, arising from the $4f \rightarrow 5d$ transition of Eu^{2+}. With the increase of Li content, the PL intensity is enhanced, which can be explained by the increase of the concentration of Eu^{2+} ions in the lattice. Thus, the internal QE is increased from 75 to 86% along with Li incorporation.

Figure 3C shows the normalized Eu-L_3 edge x-ray absorption near-edge structure (XANES) spectra of N□ASO:yLi, Eu ($0 \le y \le 0.15$). The two peaks at about 6975 and 6982 eV are attributed to the $2p_{3/2} \rightarrow 5d$
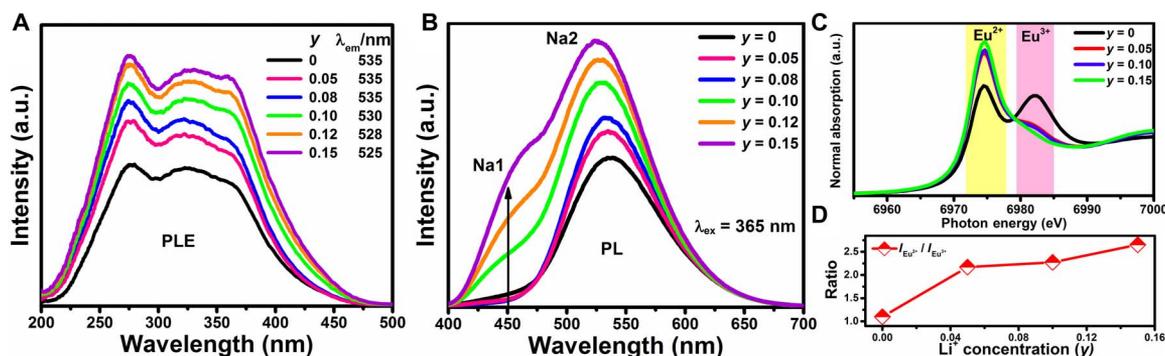
Fig. 3. PL properties of N□ASO:yLi, Eu ($0 \leq y \leq 0.15$). (**A** and **B**) PLE and PL spectra of N□ASO:yLi, Eu ($0 \leq y \leq 0.15$). Both PLE and PL spectral intensities are enhanced, and the intensity of the minor peak at ~450 nm is increased relative to that of the dominant peak at ~535 nm. (**C** and **D**) Normalized Eu L_3-edge XANES spectra and dependence of I_{Eu2+}/I_{Eu3+} on the Li$^+$ doping concentration (y) of N□ASO:yLi, Eu ($0 \leq y \leq 0.15$).

transition of Eu^{2+} and Eu^{3+}, respectively (*12*), and their intensities increase and decrease, respectively, with increasing Li concentration. Because the sum of the two peak areas is nearly constant, the peak area ratio (I_{Eu2+}/I_{Eu3+}) can be treated as the ratio of the numbers of Eu^{2+} and Eu^{3+} ions, and its variation is shown in Fig. 3D. The results confirm the positive role of Li incorporation in increasing the number of Eu^{2+} ions relative to that of Eu^{3+} ions. This is understandable because the stable oxidation state of lithium is Li$^+$, and thus, the valence electrons of Li atoms at the V_{Na1} sites would be easily donated to Eu^{3+} to reduce them into Eu^{2+}, increasing the I_{Eu2+}/I_{Eu3+} ratio.

Challenge 2: To tune PL color

The broad band at ~535 nm and the minor shoulder peak at ~450 nm can be ascribed to the two different Eu^{2+} located at Na2 and Na1 sites, respectively (*8*). When increasing the concentration of Li dopant, the intensity of the minor peak at ~450 nm is increased relatively to the dominant peak at ~535 nm, leading to a change of the emission color from yellow to green. This could be a result of Li incorporation–induced Eu^{2+} redistribution over the Na1 and Na2 sites of the host. To confirm this point, DFT calculations were performed to evaluate the relative Eu^{2+} occupancies at the Na1 and Na2 sites of the supercells without and with Li incorporation, respectively. First, for the three reference supercells without Li incorporation, a Eu atom was successively substituted for the 6 Na1 and 36 Na2 atoms, and the occurrence probability for each substitution was calculated by $P_k = \frac{1}{z_{tot}} \exp\left(-\frac{E_k}{kT}\right)$, where E_k is the DFT total energy of the doped supercell. By summing the values of P_k for the two kinds of substitutions, respectively, the occupancy ratio is Eu$_{Na1}$/Eu$_{Na2}$ = 0.029:1.000. Next, on the basis of preceding DFT calculations on N□ASO:Li$_{Al}$-2Li$_{V_{Na1}}$ supercells, six of the most stable supercells (79.2% overall occurrence probability) were chosen for the investigation of Eu substitution. By the procedure similar to that described above, the occupancy ratio is now Eu$_{Na1}$/Eu$_{Na2}$ = 0.118:1.000. Last, Eu substitutions at the Na sites of the nine most stable N□ASO:Li$_{Na}$ supercells (65.3% overall occurrence probability) were examined and the result is Eu$_{Na1}$/Eu$_{Na2}$ = 0.021:1.000. Thus, Li incorporation at Al sites induces an enhancement of Eu^{2+} occupancy at Na1 sites relative to that at Na2 sites, consistent with experimental results (Fig. 3B). It is noted for comparison that, in Eu-activated (Ba,Sr)$_{13-x}$Al$_{22-2x}$Si$_{10+2x}$O$_{66}$ phosphor, the intensity of the blue-violet emission band was increased with respect to the green emission band with increasing Sr content, which was explained as due to a redistribution of Eu^{2+} at different substitutional Ba sites (*22, 23*).

Challenge 3: To improve thermal stability

One of the requirements for LED applications is that phosphors maintain their emission intensities at elevated temperatures commonly reached in LED devices (*24*). To investigate the thermal stability of luminescence, the temperature-dependent PL spectra of N□ASO:yLi, Eu ($0 \leq y \leq 0.15$) under 365-nm excitation were measured from room temperature to 200°C with a step of 25°C, along with those of the commercial phosphor Y$_3$Al$_5$O$_{12}$:Ce^{3+} (YAG:Ce) for comparison. The detailed experimental results are given in fig. S4 (A to E), showing that the integrated intensity of the emission spectrum decreases with increasing temperature. However, the PL quenching is slower with the higher Li doping concentration (Fig. 4A). For N□ASO:yLi, Eu ($y = 0$), the PL intensity at 150°C drops by 22.4% of the initial intensity at room temperature. By contrast, for N□ASO:yLi, Eu ($y = 0.15$), only 5.4% of the initial intensity is lost, indicating an excellent thermal stability of the phosphor (Fig. 4B). The temperature dependence of the PL intensity may be described by the Arrhenius equation, $I_T = I_0/(1 + A\exp(-\Delta E/kT))$ (*25*), where I_0 is the initial intensity at room temperature, I_T is the intensity at temperature T, A is a constant, ΔE is the activation energy for thermal quenching, and k is the Boltzmann constant. The fitted ΔE value is increased from 0.24 to 0.56 eV, with increasing Li doping concentration from $y = 0$ to $y = 0.15$ (fig. S4F).

In general, the thermal quenching behavior of PL in Eu^{2+}-activated phosphors might be explained by thermal excitation of the 5d electron into the host conduction band (CB) (*26*), in which the energy difference (E_{dC}) between the emitting 5d level and the bottom of the host CB represents the activation energy. To test this mechanism, spectral measurements were first performed on Eu^{3+}-doped samples [N□ASO:yLi$^+$, Eu^{3+} ($0 \leq y \leq 0.15$)], and the results (fig. S5A) show that the charge transfer (CT) transition energies of Eu^{3+} are nearly invariant with increasing Li doping concentration. These CT energies can be taken as the energy positions (E_{Vf}) of Eu^{2+} ($4f^7$) ground state above the top of the host valence band (VB) (*27*). Next, from the excitation and emission spectra of Eu^{2+}-doped samples (Fig. 3, A and B), the Eu^{2+} 4f-5d transition energies (E_{fd}) remain similar when increasing Li doping content. Furthermore, ultraviolet–visible (UV-vis) diffuse reflectance spectral measurements of N□ASO:yLi$^+$ (fig. S5B) reveal a very slight increase of the host band gap (E_{gap}) from 4.83 eV at $y = 0$ to 4.90 eV at $y = 0.10$ (fig. S5, C to E), according to the Kubelka-Munk method and Tauc plot (*28, 29*). Combining these results, one sees that the variation of E_{dC} (= $E_{gap} - E_{Vf} - E_{fd}$) is too small to explain that of the activation energy with increasing Li doping concentration, and thus, the thermal
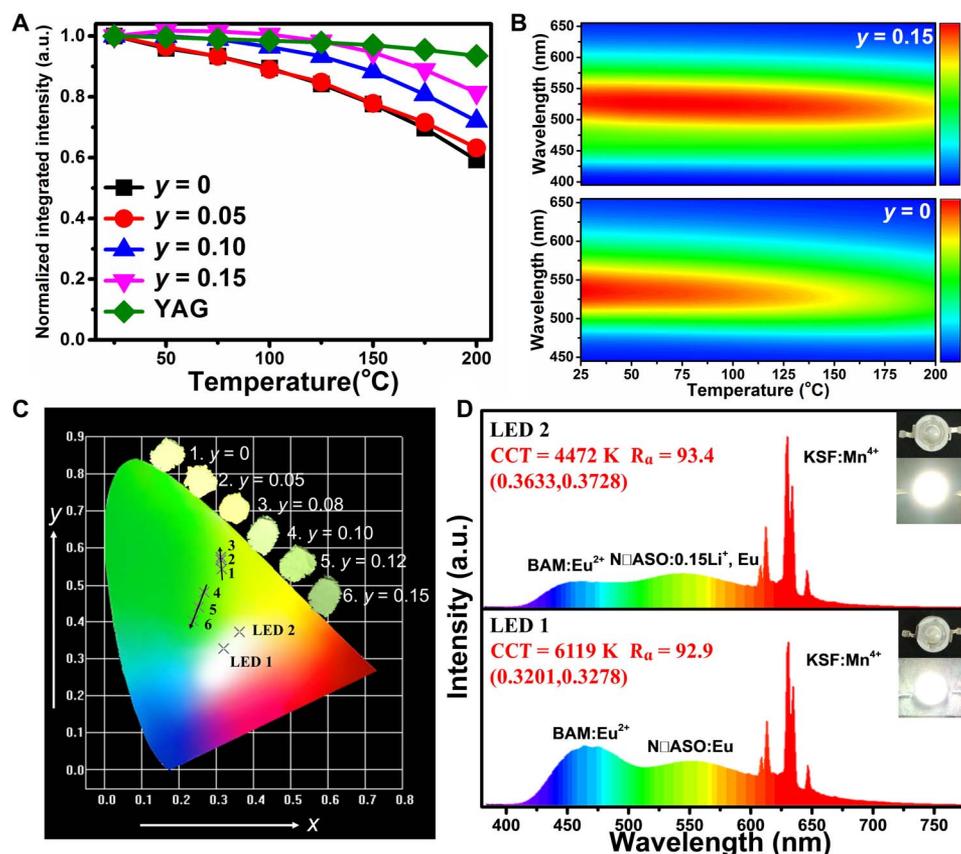
Fig. 4. Thermal quenching behavior of N□ASO:yLi, Eu ($0 \leq y \leq 0.15$) and performance of fabricated WLED devices. (**A**) Temperature-dependent normalized integrated PL intensities of the commercial phosphor YAG:Ce^{3+} and N□ASO:yLi, Eu ($0 \leq y \leq 0.15$) under 365-nm excitation, showing an improvement after doping with Li. (**B**) Temperature-dependent PL spectra of N□ASO:yLi, Eu ($y = 0, 0.15$), indicating the improved thermal stability for N□ASO:yLi, Eu ($y = 0.15$). (**C**) CIE chromaticity diagram and digital photographs of N□ASO:yLi, Eu ($0 \leq y \leq 0.15$) phosphors (λ_{ex} = 365 nm) and the fabricated WLED devices, which show a color tuning from yellow to green with increasing the doping content of Li$^+$. (**D**) Emission spectra of WLED devices fabricated with the commercial blue phosphor BAM:Eu^{2+}, the yellow/green phosphors N□ASO:Eu/N□ASO:0.15Li, Eu, and the commercial red phosphor KSF:Mn^{4+} on a near-UV LED chip (λ = 365 nm) under a current of 120 mA.

ionization mechanism can be excluded. On the basis of this observation, we propose that the higher luminescence thermal stability with more Li content is due to thermal release of more electrons from Li-related traps (e.g., Li located at V_{Na1} sites) to recombine with Eu^{3+}, resulting in excited Eu^{2+} 5d centers. The mechanism could be thermally enhanced electron transport via the host CB (*24*) or direct electron tunneling from the defect levels to Eu^{3+} centers (*30*).

Evaluation of the performance as LED phosphors

The Commission Internationale de L'Eclairage (CIE) chromaticity diagram calculated from the emission spectra of N□ASO:yLi, Eu ($0 \leq y \leq 0.15$) phosphors and their digital images upon the 365-nm UV lamp radiation are shown in Fig. 4C. All the samples can be efficiently excited by the UV light, and the emission color changes from yellow to green with increasing Li content, which demonstrates their potential application for white lighting with tunable PL. To further evaluate the commercial application of the as-synthesized N□ASO:yLi, Eu ($0 \leq y \leq 0.15$) phosphors, we fabricated WLEDs by combining the commercial blue phosphor BaMgAl$_{10}$O$_{17}$:Eu^{2+} (BAM:Eu^{2+}), the yellow/green phosphors N□ASO:Eu/N□ASO:0.15Li, Eu, the red phosphor K$_2$SiF$_6$:Mn^{4+} (KSF: Mn^{4+}), and a near-UV LED chips (λ = 365 nm) under various drive currents. The photoelectric properties, including the emission spectra,

color correlated temperature (CCT), color rendering index (R_a), luminous efficacy, and CIE color coordinates of the WLEDs are listed in tables S4 and S5. Figure 4D shows the EL spectra of the fabricated LED 1 (using the yellow phosphors N□ASO:Eu) and LED 2 (using the green phosphors N□ASO:Li, Eu) devices under a current of 120 mA, and the inset shows the photographs of the LED devices. The color rendering index values of both LEDs are very high (R_a = 92.9 and 93.4 for LED 1 and 2, respectively), and the CCT could be tuned (6119 and 4472 K for LED 1 and LED 2, respectively). Therefore, the WLED devices fabricated using N□ASO:yLi, Eu phosphors can exhibit tunable properties for different solid-state lighting applications.

In summary, we have presented a useful strategy that enables us to optimize the efficiency of single-phase phosphors, tune the PL color, and improve their thermal stability with Li doping. This approach has been illustrated with N□ASO:yLi, Eu ($0 \leq y \leq 0.15$) phosphors. Under the excitation of 365 nm, these phosphors exhibited two emission peaks centered at ~450 and ~535 nm. The intensity of the former emission peak was enhanced relative to the latter, with the increase of Li content due to an increase of Eu^{2+} occupation at Na1 sites relative to Na2 sites, as corroborated by DFT calculations. Meanwhile, an overall increase of the excitation and emission intensities owing to improved reduction of Eu^{3+} to Eu^{2+} was confirmed by XANES measurements.

Moreover, the Li incorporation improved the thermal stability of the phosphors as a result of the interplay with Li-related electron traps. Last, by using the Li-doped NaAlSiO$_4$:Eu^{2+} as a green light component, the WLED devices with tuning properties could be obtained. The present work demonstrates that killing three birds with one stone [i.e., (i) optimizing PL efficiency, (ii) tuning emission color, and (iii) improving thermal stability] by only Li doping into a preselected phosphor is a promising strategy for the exploration of phosphors with better luminescence performance.

MATERIALS AND METHODS

Materials and preparation

The powder samples of N□ASO:yLi, Eu ($x = y$, $0 \leq y \leq 0.15$), N□$_x$ ASO ($0 \leq x \leq 0.25$), and N□$_x$ ASO:Eu ($0 \leq x \leq 0.25$) were prepared by the solution method using proper amounts of Al(NO$_3$)$_3$ 9H$_2$O (A.R., Aladdin), NaNO$_3$ (A.R., Aladdin), LiNO$_3$ (A.R., Aladdin), Si(OC$_2$H$_5$)$_4$ (TEOS; 99.999%, Aladdin), and Eu(NO$_3$)$_3$ 6H$_2$O (99.9%, Aladdin) as starting materials. For N□$_x$ ASO ($x = 0$), the ratio of the starting materials of NaNO$_3$, Al(NO$_3$)$_3$ 9H$_2$O, and TEOS is determined as 1.4:1.4:1. All reactants were dissolved in water (solution A) except for TEOS, which was mixed with ethanol (solution B). Solutions A and B were then thoroughly mixed together. The mixtures were dehydrated in an oven at 120°C until the solvent evaporated completely (31). The dried samples were ground into fine powders and then sintered at 1200°C for 4 hours in a tube furnace under a reducing atmosphere of N$_2$-H$_2$ (5%). Then, the samples were cooled to room temperature in the furnace and were reground for further analysis.

Characterization

The laboratory PXRD patterns for phase identification and Rietveld analysis were recorded using a D8 Advance diffractometer (Bruker Corporation, Germany) operating at 40 kV and 40 mA with monochromatized Cu Kα radiation ($\lambda = 1.5406$ Å). SXRD data for Rietveld analysis were collected by a synchrotron device of TPS 09A high-resolution powder diffraction end station ($\lambda = 0.82656$ Å, 15 keV) and MYTHEN 24K detector in the National Synchrotron Radiation Research Center, Taiwan. The step size of 2θ was 0.00375°, and the exposition time was 60 s. Rietveld refinement was performed by using TOPAS 4.2 software (32). The optical microscope photographs of the powder sample were obtained by using a Nikon LV100ND optical microscope. The morphology and size of the powder sample were characterized by SEM (JEOL JSM-6510). The elemental mapping was obtained using EDS that was attached to the SEM. TEM images were characterized by a JEOL JEM-2010 microscope, with an accelerated voltage of 200 kV. ^{7}Li/^{26}Al/^{29}Si solid-state NMR spectra were obtained on JNM-ECZ600R at 15 kHz. The external reference for ^{7}Li was LiCl, Al(NO$_3$)$_3$ 9H$_2$O for ^{26}Al, and SiO$_2$ for ^{29}Si.

The PL and PLE spectra at room temperature were performed in a fluorescence spectrophotometer (F-4600, Hitachi, Japan) equipped with a photomultiplier tube operating at 400 V and a 150-W Xe lamp as the excitation source. The temperature-dependent spectra were measured by the same instrument equipped with a heating apparatus. The internal QE was measured by a fluorescence spectrophotometer (FLS920, Edinburgh Instruments Ltd., UK), where the Xe900 lamp was used as an excitation source and the white BaSO$_4$ powder was used as a reference for correction of absorption. The XANES of Eu L_3-edge was obtained on the 1W2B beamline of the Beijing Synchrotron Radiation Facility. The diffuse reflectance spectra at room temperature were

measured on an UV-vis near-infrared spectrophotometer (UH4150, Hitachi, Japan).

WLED fabrication

WLEDs were fabricated with the commercial blue phosphor BAM:Eu^{2+}, the yellow or green phosphors N□ASO:Eu or N□ASO:0.15Li, Eu, the red phosphor KSF:Mn^{4+}, and a near-UV LED chips ($\lambda = 365$ nm). The phosphors were thoroughly mixed with epoxy resin, and the obtained phosphor-epoxy resin mixture was coated on the LED chips. The photoelectric properties, including the emission spectra, CCT, color rendering index (R_a), luminous efficacy, and CIE color coordinates of the WLEDs, were measured by using an integrating sphere spectroradiometer system (ATA-1000, EVER FINE).

Computational methodology

Periodic DFT calculations were performed using the Perdew-Burke-Ernzerhof (PBE) functional (33) and its PBE + U variant with U_{eff} = 2.5 eV for the Eu 4f electrons(34, 35), as implemented in the Vienna Ab initio Simulation Package (VASP) code (36, 37). Na(2$p^6$3s^1), Al(3$s^2$3p^1), Si(3$s^2$3p^6), O(2$s^2$2p^4), Li(1$s^2$2s^1), and Eu(5$s^2$5$p^6$4$f^7$6s^2) were treated as valence electrons, and their interactions with the cores were described by the projected augmented wave approach (38). To investigate Li and Eu incorporations in the material, a reference $1 \times 1 \times 2$ supercell (109 atoms) for undoped N□ASO was first constructed. For the supercells with Eu^{2+} located at a Na$^+$ site, the excess charge was compensated by introducing a uniform background charge density. The atomic structures of undoped and doped supercells were fully optimized until the total energies and the forces on the atoms converged to 10^{-6} eV and 0.01 eV Å^{-1}. A $2 \times 2 \times 2$ k-point grid was used, and the cutoff energy for the plane wave basis was set to 530 eV.

The formation energy (E_i) for Li situated at a host site (X) of N□ASO was calculated by

$$E_i = E(\text{N□ASO} : \text{Li}_X) - E(\text{N□ASO}) + \mu_X - \mu_{\text{Li}}$$

where E is the total energy of the supercell and μ is the chemical potential of the atom. Because the material was synthesized in reducing atmosphere, the energy of a metallic atom may approximate the corresponding chemical potential of the atom in N□ASO. Calculations for metallic Na (2-atom cell), Al (4-atom cell), and Li (2-atom cell) were performed with the same convergence criteria as above and a $16 \times 16 \times 16$ k-point grid.

SUPPLEMENTARY MATERIALS

Supplementary material for this article is available at http://advances.sciencemag.org/cgi/content/full/5/1/eaav0363/DC1

Fig. S1. Rietveld refinement of N□$_x$ASO and N□$_x$ASO:Eu.

Fig. S2. Rietveld refinement of N□ASO:yLi, Eu.

Fig. S3. ^{27}Al and ^{29}Si NMR of N□ASO:yLi, Eu and N□$_x$ASO.

Fig. S4. Thermal quenching behavior of YAG:Ce and N□ASO:yLi, Eu.

Fig. S5. The CT transition energies of Eu^{3+} and the band gap calculation of the N□ASO:yLi host.

Table S1. Main parameters of processing and refinement of the N□$_x$ASO ($0 \leq x \leq 0.25$) and N□$_x$ASO:Eu ($0 \leq x \leq 0.25$) samples.

Table S2. Main parameters of processing and refinement of the N□ASO:yLi, Eu ($0 \leq y \leq 0.15$) samples.

Table S3. Fractional atomic coordinates and isotropic displacement parameters (Å^2) of the N□ASO:yLi, Eu ($0 \leq y \leq 0.15$) samples.

Table S4. The photoelectric properties of WLEDs fabricated using yellow-emitting N□ASO:Eu phosphor, blue-emitting commercial BAM:Eu^{2+}, and red-emitting commercial KSF:Mn^{4+} phosphor with a near-UV LED chip ($\lambda = 365$ nm) excitation under various drive currents.

Table S5. Photoelectric properties of WLEDs fabricated using green-emitting N□ASO:0.15Li, Eu phosphor, blue-emitting commercial BAM:Eu^{2+}, and red-emitting commercial KSF:Mn^{4+} phosphor with a near-UV LED chip ($\lambda = 365$ nm) excitation under various drive currents.

REFERENCES AND NOTES

1. E. F. Schubert, J. K. Kim, Solid-state light sources getting smart. *Science* **308**, 1274–1278 (2005).

2. P. Pust, P. J. Schmidt, W. Schnick, A revolution in lighting. *Nat. Mater.* **14**, 454–458 (2015).

3. X. Qin, X.-W. Liu, W. Huang, M. Bettinelli, X.-G. Liu, Lanthanide-activated phosphors based on 4f-5d optical transitions: Theoretical and experimental aspects. *Chem. Rev.* **117**, 4488–4527 (2017).

4. N. C. George, K. A. Denault, R. Seshadri, Phosphors for solid-state white lighting. *Annu. Rev. Mater. Sci.* **43**, 481–501 (2013).

5. H. Zhu, C. C. Lin, W. Luo, S. Shu, Z. Liu, Y. Liu, J. Kong, E. Ma, Y. Cao, R.-S. Liu, X. Chen, Highly efficient non-rare-earth red emitting phosphor for warm white light-emitting diodes. *Nat. Commun.* **5**, 4312 (2014).

6. Z. Xia, Q. Liu, Progress in discovery and structural design of color conversion phosphors for LEDs. *Prog. Mater. Sci.* **84**, 59–117 (2016).

7. P. Pust, V. Weiler, C. Hecht, A. Tucks, A. S. Wochnik, A.-K. Henß, D. Wiechert, C. Scheu, P. J. Schmidt, W. Schnick, Narrow-band red-emitting Sr[LiAl₃N₄]:Eu²⁺ as a next-generation LED-phosphor material. *Nat. Mater.* **13**, 891–896 (2014).

8. M. Zhao, Z. Xia, M. S. Molokeev, L. Ning, Q. Liu, Temperature and Eu²⁺-doping induced phase selection in NaAlSiO₄ polymorphs and the controlled yellow/blue emission. *Chem. Mater.* **29**, 6552–6559 (2017).

9. S. P. Ong, Z.-B. Wang, J. Ha, Y. H. Kim, W.-B. Im, J. McKittrick, Mining unexplored chemistries for phosphors for high-color-quality white-light-emitting diodes. *Bull. Am. Phys. Soc.* (2018).

10. Z. Xia, G. Liu, J. Wen, Z. Mei, M. Balasubramanian, M. S. Molokeev, L. Peng, L. Gu, D. J. Miller, Q. Liu, K. R. Poeppelmeier, Tuning of photoluminescence by cation nanosegregation in the (CaMg)ₓ(NaSc)₁₋ₓSi₂O₆ solid solution. *J. Am. Chem. Soc.* **138**, 1158–1161 (2016).

11. L. Wang, R.-J. Xie, Y. Li, X. Wang, C.-G. Ma, D. Luo, T. Takeda, Y.-T. Tsai, R.-S. Liu, N. Hirosaki, Ca₁₋ₓLiₓAl₁₋ₓSi₁₊ₓN₃:Eu²⁺ solid solutions as broadband, color-tunable and thermally robust red phosphors for superior color rendition white light-emitting diodes. *Light Sci. Appl.* **5**, e16155 (2016).

12. S. Li, L. Wang, D. Tang, Y. Cho, X. Liu, X. Zhou, L. Lu, L. Zhang, T. Takeda, N. Hirosaki, R.-J. Xie, Achieving high quantum efficiency narrow-band β-Sialon:Eu²⁺ phosphors for high-brightness LCD backlights by reducing the Eu³⁺ luminescence killer. *Chem. Mater.* **30**, 494–505 (2018).

13. Y. Sato, H. Kato, M. Kobayashi, T. Masaki, D.-H. Yoon, M. Kakihana, Tailoring of deep-red luminescence in Ca₂SiO₄:Eu²⁺. *Angew. Chem. Int. Ed.* **53**, 7756–7759 (2014).

14. Y. H. Kim, P. Arunkumar, B. Y. Kim, S. Unithrattil, E. Kim, S.-H. Moon, J. Y. Hyun, K. H. Kim, D. Lee, J.-S. Lee, W. B. Im, A zero-thermal-quenching phosphor. *Nat. Mater.* **16**, 543–550 (2017).

15. K. A. Denault, J. Brgoch, M. W. Gaultois, A. Mikhailovsky, R. Petry, H. Winkler, S. P. DenBaars, R. Seshadri, Consequences of optimal bond valence on structural rigidity and improved luminescence properties in SrₓBa₂₋ₓSiO₄:Eu²⁺ orthosilicate phosphors. *Chem. Mater.* **26**, 2275–2282 (2014).

16. H. Terraschke, C. Wickleder, UV, blue, green, yellow, red, and small: Newest developments on Eu²⁺-doped nanophosphors. *Chem. Rev.* **115**, 11352–11378 (2015).

17. W. A. Dollase, W. M. Thomas, The crystal chemistry of silica-rich, alkali-deficient nepheline. *Contrib. Mineral. Petrol.* **66**, 311–318 (1978).

18. Y. Guo, X. Yu, J. Liu, X. Yang, Photoluminescence of Eu²⁺-activated Na₁₋ₓAl₁₋ₓSi₁₊ₓO₄ upon UV excitation. *J. Rare Earths* **28**, 34–36 (2010).

19. A. Kumar, S. J. Dhoble, D. R. Peshwe, J. Bhatt, Structural and photoluminescence properties of nepheline-structure NaAlSiO₄:Dy³⁺ nanophosphors. *J. Alloys Compd.* **609**, 100–106 (2014).

20. M. E. Smith, K. J. D. Mackenzie, *Multinuclear Solid-State NMR of Inorganic Materials* (Pergamon Materials Series, Elsevier Science, 2002).

21. R. Grau-Crespo, S. Hamad, C. R. A. Catlow, N. H. de Leeuw, Symmetry-adapted configurational modelling of fractional site occupancy in solids. *J. Phys. Condens. Matter* **19**, 256201 (2007).

22. G. Denis, P. Deniard, E. Gautron, F. Clabau, A. Garcia, S. Jobic, Structure and white luminescence of Eu-activated (Ba,Sr)₁₃₋ₓAl₂₂₋₂ₓSi₁₀₊₂ₓO₆₆ materials. *Inorg. Chem.* **47**, 4226–4235 (2008).

23. G. Denis, X. Rocquefelte, P. Deniard, M.-H. Whangbo, S. Jobic, Site preference of Eu²⁺ dopants in the (Ba,Sr)₁₃₋ₓAl₂₂₋₂ₓSi₁₀₊₂ₓO₆₆ phosphor and its effect on the luminescence properties: A density functional investigation. *J. Mater. Chem.* **19**, 9170–9175 (2009).

24. J. Qiao, L. Ning, M. S. Molokeev, Y.-C. Chuang, Q. Liu, Z. Xia, Eu²⁺ site preferences in the mixed cation K₂BaCa(PO₄)₂ and thermally stable luminescence. *J. Am. Chem. Soc.* **140**, 9730–9736 (2018).

25. S. Bhushan, M. V. Chukichev, Temperature dependent studies of cathodoluminescence of green band of ZnO crystals. *J. Mater. Sci. Lett.* **7**, 319–321 (1988).

26. P. Dorenbos, Thermal quenching of Eu²⁺ 5d–4f luminescence in inorganic compounds. *J. Phys. Condens. Matter* **17**, 8103 (2005).

27. P. Dorenbos, Systematic behaviour in trivalent lanthanide charge transfer energies. *J. Phys. Condens. Matter* **15**, 8417 (2003).

28. J. H. Nobbs, Kubelka–Munk theory and the prediction of reflectance. *Cold Reg. Sci. Technol.* **15**, 66–75 (1985).

29. E. J. Johnson, in *Semiconductors and Semimetals* (Elsevier, 1967), vol. 3, pp. 153–258.

30. C. C. Lin, Y.-T. Tsai, H. E. Johnston, M.-H. Fang, F. Yu, W. Zhou, P. Whitfield, Y. Li, J. Wang, R.-S. Liu, J. P. Attfield, Enhanced photoluminescence emission and thermal stability from introduced cation disorder in phosphors. *J. Am. Chem. Soc.* **139**, 11766–11770 (2017).

31. J. Y. Han, W. B. Im, D. Kim, S. H. Cheong, G.-Y. Lee, D. Y. Jeon, New full-color-emitting phosphor, Eu²⁺-doped Na₂₋ₓAl₂₋ₓSiₓO₄ (0 ≤ x ≤ 1), obtained using phase transitions for solid-state white lighting. *J. Mater. Chem.* **22**, 5374–5381 (2012).

32. Bruker AXS, *TOPAS V4: General Profile and Structure Analysis Software for Powder Diffraction Data: User's Manual* (Bruker AXS, 2008).

33. J. P. Perdew, K. Burke, M. Ernzerhof, Generalized gradient approximation made simple. *Phys. Rev. Lett.* **77**, 3865–3868 (1996).

34. A. Canning, A. Chaudhry, R. Boutchko, N. Grønbech-Jensen, First-principles study of luminescence in Ce-doped inorganic scintillators. *Phys. Rev. B* **83**, 125115 (2011).

35. S. L. Dudarev, G. A. Botton, S. Y. Savrasov, C. J. Humphreys, A. P. Sutton, Electron-energy-loss spectra and the structural stability of nickel oxide: An LSDA+U study. *Phys. Rev. B* **57**, 1505 (1998).

36. G. Kresse, J. Furthmüller, Efficient iterative schemes for ab initio total-energy calculations using a plane-wave basis set. *Phys. Rev. B* **54**, 11169 (1996).

37. G. Kresse, D. Joubert, From ultrasoft pseudopotentials to the projector augmented-wave method. *Phys. Rev. B* **59**, 1758 (1999).

38. P. E. Blöchl, Projector augmented-wave method. *Phys. Rev. B* **50**, 17953 (1994).

ScienceAdvances

Li substituent tuning of LED phosphors with enhanced efficiency, tunable photoluminescence, and improved thermal stability

Ming Zhao, Zhiguo Xia, Xiaoxiao Huang, Lixin Ning, Romain Gautier, Maxim S. Molokeev, Yayun Zhou, Yu-Chun Chuang, Qinyuan Zhang, Quanlin Liu and Kenneth R. Poeppelmeier

ARTICLE TOOLS	http://advances.sciencemag.org/content/5/1/eaav0363
SUPPLEMENTARY MATERIALS	http://advances.sciencemag.org/content/suppl/2019/01/07/5.1.eaav0363.DC1
REFERENCES	This article cites 34 articles, 1 of which you can access for free http://advances.sciencemag.org/content/5/1/eaav0363#BIBL
PERMISSIONS	http://www.sciencemag.org/help/reprints-and-permissions

Use of this article is subject to the Terms of Service